AIAA JOURNAL
Vol. 42, No. 2, February 2004

Sound Generation by Vortex Pairing in Subsonic Axisymmetric Jets

X. Jiang,* E. J. Avital,† and K. H. Luo‡
University of London, London, England E1 4NS, United Kingdom

Direct numerical simulation (DNS) and an acoustic analogy are used to investigate the sound generation by vortex pairing in idealized subsonic axisymmetric jets. The detailed sound source structure is provided by the DNS. The acoustic analogy is based on solving the nonlinearized Lilley's third-order wave equation in the time-space domain. A numerical algorithm for solving Lilley's equation is developed, in which the sound field is simulated simultaneously with the source field calculation. The computational domain includes both the near field and a portion of the acoustic far field. Effects of a coaxial secondary jet stream and the jet-to-ambient temperature ratio on the sound generation from an axisymmetric jet are investigated. It is shown that the sound source has a long axial distribution in the streamwise direction with the strongest source located near the end of the jet potential core where vortex pairing/merging occurs, and the radiated sound field is highly directive. It is also found that the secondary jet stream reduces the sound source size; therefore, the sound radiation from the coaxial jets is lower than that from the single jet. The hot jet simulation shows that increasing the jet-to-ambient temperature ratio leads to a smaller and weaker sound source, but does not lead to a weaker sound field. For the sound field a reasonable agreement is observed between the predictions from the axisymmetric Lilley's equation and the DNS results.

I. Introduction

INTEREST in sound generation from subsonic jets is associated with a broad range of aerodynamic applications. The sound associated with vortical structures in the flowfield is a major component of subsonic jet noise. Jet noise has been the subject of numerous studies,[1–8] and sound generation by vortex pairing in subsonic jets has been investigated both experimentally and computationally.[2,3] Recently, it was demonstrated that the addition of a coaxial subsonic secondary jet stream to a supersonic jet stream can reduce the Mach wave emission of the primary supersonic jet.[4,5] Subsonic coaxial jets are also encountered in many aeronautical applications. However, sound generation from subsonic coaxial jets received little attention in the past.

Another important issue in subsonic jet noise prediction is the temperature effect on the sound generation. Hot jets are encountered in many energy-producing aeronautical systems such as the propulsion system. Nevertheless, most of the existing studies concentrated on jets without significant temperature differences. There were relatively less studies done on noise from hot jets. Sound generation from hot jets including that from reacting jets remains an area requiring further investigations.[6,7]

For aeroacoustic noise predictions of jets, the traditional methods relied primarily on qualitative theoretical calculations and experimental observations. Because of the difficulties in getting the detailed sound source structure, accurate quantitative predictions were hard to achieve. Computational aeroacoustics (CAA) has been developing rapidly in recent years because of the significant advancement in both computer power and numerical methods. Particularly, direct numerical simulations provide a possibility to yield more fundamental knowledge about the sound generation process. This is mainly because direct numerical simulation (DNS) provides detailed information on the sound source structure by resolving all of the relevant timescales and length scales of the source flowfield.

A useful approach for aeroacoustic predictions of subsonic jets is to compute the near-field hydrodynamic region with Navier–Stokes equations and use an acoustic analogy to determine the far-field sound. As a tool of sound predictions, Lighthill's analogy[9] was the starting point of computational aeroacoustics. It has been widely used in jet noise predictions. Other acoustic analogies were also developed, for instance, Lilley's third-order acoustic analogy equation.[1] Lilley's equation was anticipated to improve the sound predictions by reducing the cancelation effects in the source terms, especially to improve predictions of the high-frequency sound-wave scattering and refraction. It was pointed out[10] that certain jet noise features could be well explained by solutions of Lilley's equation, such as the enhanced directionality (over predictions based on Lighthill's equation) and the zone of silence along the downstream axis for high frequencies. For hot jets it is believed that Lilley's acoustic analogy equation is more appropriate than Lighthill's equation because the large sound speed difference inside the jet shear layer makes the sound refraction effects more prominent.

For the application of Lilley's equation, the common approach was to linearize it about a time-independent parallel base flow. This linearization, however, could blur the distinction between the propagation and source terms.[11] Recently, Colonius et al.[12] used DNS of the unsteady Navier–Stokes equations to compute the acoustic field of a two-dimensional planar mixing layer and compared the results with acoustic predictions from Lilley's equation. In their work the linearized Lilley's equation was solved in the frequency-space domain. Because the Fourier transform in time was used, only the sound that was produced after a periodic state had been reached was considered. They found that the presence of flow-acoustic interactions in the computed source terms caused the acoustic field predicted by the acoustic analogy to be very sensitive to small changes in the description of the source. Attempts to take the nonlinear propagation terms as sources could result in a deterioration of the numerical accuracy.

This study is devoted to a better understanding of sound generation from vortical structures in subsonic jets. Particular attention

Presented as Paper 2002-2531 at the AIAA/CEAS 8th Aeroacoustics Conference, Breckenridge, CO, 17–19 June 2002; received 23 March 2003; revision received 18 July 2003; accepted for publication 18 July 2003.

*Postdoctoral Research Associate, Department of Engineering, Queen Mary, Mile End Road; currently Lecturer, Department of Mechanical Engineering, Brunel University, Uxbridge, England UB8 3PH, United Kingdom; xi.jiang@brunel.ac.uk.

†Lecturer, Department of Engineering, Queen Mary, Mile End Road. Member AIAA.

‡Professor, Department of Engineering, Queen Mary, Mile End Road. Member AIAA.

has been given to the effects of a coaxial secondary jet stream and the jet-to-ambient temperature ratio on the sound generation by vortex pairing in an idealized axisymmetric jet. In the simulations performed, the detailed sound source structure is provided by the near-field DNS, whereas the sound field is obtained from both the DNS and the numerical solution of Lilley's equation. Unlike the previous study,[12] the third-order Lilley's equation is solved in the time-space domain. The sound field is simulated simultaneously with the source-field DNS, by using a time-marching technique. In this way the retarded-time variation can be easily accounted for. To avoid the ambiguity associated with the linearization, the nonlinearized Lilley's equation is adopted. By using the nonlinearized Lilley's equation, the effects of jet spreading and merging of the primary and secondary jet streams of the coaxial jets on the sound generation can be taken into account.

A comparative study has been performed to examine the sound generation by vortex pairing in the relatively low-Reynolds-number subsonic jets. Results from three computational cases are presented: a single jet without temperature difference, coaxial jets with the secondary/primary mean-velocity ratio 0.4 and without temperature difference, and a single hot jet with the jet-to-ambient temperature ratio 2. Because the requirement on computational resources of computing the jet near and far fields together is very large, therefore only an axisymmetric flow is considered in this study. This allows a relatively large portion of the acoustic field to be computed and the flow features to be well resolved.

II. Mathematical Formulation

A. Flow Equations for the DNS

The flowfield is described with the compressible time-dependent Navier–Stokes equations for the idealized axisymmetric jet. The physical space is spanned by a stationary cylindrical coordinate system (x, r, θ), where x is along the jet axis. In this work the nondimensional form of the governing equations is employed. Major reference quantities used in the normalization of the governing equations are the initial centerline velocity, radius of the primary jet, and the ambient temperature and density. The nondimensional quantities are x, streamwise distance; r, radial distance; u_x, streamwise velocity; u_r, radial velocity; c, sonic speed; e, internal energy per unit mass; $E_T = \rho[e + (u_x^2 + u_r^2)/2]$, total energy; M, Mach number; p, pressure; Pr, Prandtl number; Re, Reynolds number; t, time; T, temperature; μ, dynamic viscosity; and ρ, density.

The conservation laws for mass, momentum, and energy can be written in the following form for the axisymmetric cylindrical coordinates:

$$\frac{\partial \boldsymbol{Q}}{\partial t} = -\frac{\partial \boldsymbol{E}}{\partial x} - \frac{1}{r}\frac{\partial (\boldsymbol{F}r)}{\partial r} - \boldsymbol{G} \tag{1}$$

where vectors $\boldsymbol{Q}$, $\boldsymbol{E}$, $\boldsymbol{F}$, and $\boldsymbol{G}$ are defined as

$$\boldsymbol{Q} = \begin{pmatrix} \rho \\ \rho u_x \\ \rho u_r \\ E_T \end{pmatrix} \tag{2}$$

$$\boldsymbol{E} = \begin{bmatrix} \rho u_x \\ \rho u_x^2 + p - \tau_{xx} \\ \rho u_x u_r - \tau_{xr} \\ (E_T + p)u_x + q_x - u_x\tau_{xx} - u_r\tau_{xr} \end{bmatrix} \tag{3}$$

$$\boldsymbol{F} = \begin{bmatrix} \rho u_r \\ \rho u_x u_r - \tau_{xr} \\ \rho u_r^2 + p - \tau_{rr} \\ (E_T + p)u_r + q_r - u_r\tau_{rr} - u_x\tau_{xr} \end{bmatrix} \tag{4}$$

$$\boldsymbol{G} = \begin{bmatrix} 0 \\ 0 \\ (-p + \tau_{\theta\theta})/r \\ 0 \end{bmatrix} \tag{5}$$

The constitutive relations for viscous stress τ_{xx}, τ_{rr}, $\tau_{\theta\theta}$, τ_{xr}, and heat-flux components q_x, q_r were given in Ref. 13.

For the axisymmetric jet it is preferable to include the centerline into the mathematical formulation. This has the advantage of applying the symmetry conditions precisely. At the centerline a new set of equations was derived from the original equations by using l'Hôpital's rule to circumvent the singularity in the formulation. The new set of governing equations can be found in Ref. 13.

The flow equations also include the perfect gas law, which is given by

$$p = \rho T/\gamma M^2 \tag{6}$$

where γ is the ratio of specific heats.

B. Acoustic Analogy Equation

Lilley's third-order wave equation[1] can be obtained by combining the equations describing conservation of mass and momentum for compressible flow. In this study the nonlinearized Lilley's equation is adopted to avoid the ambiguity associated with the assumption of a time-independent parallel mean flow for the jet.

In the derivation of Lilley's equation, it is convenient to define a logarithmic pressure variable:

$$\Pi = \ell_n(p/p_a) \tag{7}$$

where $p_a = 1/(\gamma M^2)$ is the ambient pressure. From the continuity and momentum equations Lilley's equation in the axisymmetric cylindrical coordinates can be derived as

$$\frac{\mathrm{D}}{\mathrm{D}t}\left[\frac{\mathrm{D}^2\Pi}{\mathrm{D}t^2} - \frac{1}{r}\frac{\partial}{\partial x_i}\left(rc^2\frac{\partial \Pi}{\partial x_i}\right)\right] + 2\frac{\partial u_i}{\partial x_j}\frac{\partial}{\partial x_i}\left(c^2\frac{\partial \Pi}{\partial x_j}\right) + 2c^2\frac{u_r}{r^2}\frac{\partial \Pi}{\partial r} = -2\gamma\frac{\partial u_i}{\partial x_j}\frac{\partial u_k}{\partial x_i}\frac{\partial u_j}{\partial x_k} - 2\gamma\frac{u_r^3}{r^3} \tag{8}$$

where $\mathrm{D}/\mathrm{D}t = \partial/\partial t + u_i\partial/\partial x_i$ is the convective derivative. For an axisymmetric flow $\mathrm{D}/\mathrm{D}t = \partial/\partial t + u_x\partial/\partial x + u_r\partial/\partial r$, while the different terms in Eq. (8) can be given by

$$\frac{1}{r}\frac{\partial}{\partial x_i}\left(rc^2\frac{\partial \Pi}{\partial x_i}\right) = c^2\left(\frac{\partial^2\Pi}{\partial x^2} + \frac{\partial^2\Pi}{\partial r^2} + \frac{1}{r}\frac{\partial \Pi}{\partial r}\right) + \frac{\partial c^2}{\partial x}\frac{\partial \Pi}{\partial x} + \frac{\partial c^2}{\partial r}\frac{\partial \Pi}{\partial r} \tag{9}$$

$$\frac{\partial u_i}{\partial x_j}\frac{\partial}{\partial x_i}\left(c^2\frac{\partial \Pi}{\partial x_j}\right) = c^2\left[\frac{\partial u_x}{\partial x}\frac{\partial^2\Pi}{\partial x^2} + \left(\frac{\partial u_x}{\partial r} + \frac{\partial u_r}{\partial x}\right)\frac{\partial^2\Pi}{\partial x\partial r} + \frac{\partial u_r}{\partial r}\frac{\partial^2\Pi}{\partial r^2}\right] + \frac{\partial c^2}{\partial x}\left(\frac{\partial u_x}{\partial x}\frac{\partial \Pi}{\partial x} + \frac{\partial u_x}{\partial r}\frac{\partial \Pi}{\partial r}\right) + \frac{\partial c^2}{\partial r}\left(\frac{\partial u_r}{\partial x}\frac{\partial \Pi}{\partial x} + \frac{\partial u_r}{\partial r}\frac{\partial \Pi}{\partial r}\right) \tag{10}$$

$$\frac{\partial u_i}{\partial x_j}\frac{\partial u_k}{\partial x_i}\frac{\partial u_j}{\partial x_k} = \left(\frac{\partial u_x}{\partial x}\frac{\partial u_x}{\partial x} + 2\frac{\partial u_x}{\partial r}\frac{\partial u_r}{\partial x} + \frac{\partial u_r}{\partial r}\frac{\partial u_r}{\partial r}\right) \times \left(\frac{\partial u_x}{\partial x} + \frac{\partial u_r}{\partial r}\right) \tag{11}$$

In Eq. (8) the left-hand side is considered to be the wave operator that contains the pressure variable Π, whereas the right-hand side is taken as the sound source. The wave operator in the left-hand side of Lilley's equation includes the refraction and sound speed effects. By applying l'Hôpital's rule, the singularity of Eq. (8) at $r=0$ can also be circumvented. The special form of the axisymmetric Lilley's equation at the jet centerline in given in the Appendix.

In this study Lilley's equation is solved simultaneously with the DNS, where the DNS provides the flowfield and the sound source structure for the numerical solution of Lilley's equation. In a more general situation Lilley's equation can also be solved to predict the sound field with known knowledge on the sound source and flowfield from other approaches.

III. Numerical Implementation

The computational domain includes both the near field and a significant portion of the acoustic far field. The dimensions of the computational domain are $0 \le x \le L_x$ and $0 \le r \le L_r$. In the axial direction a sponge layer $L_{xp} < x \le L_x$ is used to prevent the spurious wave reflections from the outflow boundary.[13] Therefore only the region $0 \le x \le L_{xp}$ is considered to contain physically meaningful data. A grid system uniformly spaced in the x direction and nonequally spaced in the r direction is used. The mapped grid in the radial direction is employed to resolve the jet near-field flow structure and far-field sound more efficiently, which is of the form used by Avital.[14] It includes an inner block for the hydrodynamic region with stretched points and an outer block with equally spaced points. Details of the grid stretching used can be found in Ref. 14.

In the simulations performed both the flow equations for the DNS and the axisymmetric Lilley's acoustic analogy equation are solved in the time-space domain. To avoid the risk of the numerical discretization distorting the sound field, high-order numerical methods and the appropriate boundary conditions are used.

A. Numerical Methods for the DNS

The numerical methods used include the spatial differentiation and time-integration schemes and the implementation of boundary conditions. Spatial differentiation of the governing equation is performed using a sixth-order-accurate compact (Padé) finite difference scheme with spectral-like resolution,[15] which is of sixth order at inner points, fourth order at the next to boundary points, and third order at the boundary. This numerical scheme allows more flexibility in the specification of boundary conditions with minimal loss of accuracy compared to spectral methods. At the jet centerline $r=0$, the formal sixth-order accuracy of the numerical scheme is preserved by applying the symmetry conditions to both the primitive variables and their first and second derivatives in the radial direction.[13] The time-dependent governing equations are integrated forward in time using a third-order compact-storage fully explicit Runge–Kutta scheme[16] of the family derived by Wray (Wray, A. A., "Very Low Storage Time-Advanced Schemes," NASA Internal Report, 1986, private communication).

There are four boundaries for the computational box, which is a rectangle that represents half of a cross section of the axisymmetric domain, including 1) an inflow boundary at the domain inlet $x=0$; 2) an outflow boundary downstream of the computational domain $x=L_x$; 3) the far side boundary in the radial direction $r=L_r$; and 4) the symmetry boundary at the centerline $r=0$. The symmetry conditions are applied at the jet centerline without additional characteristic boundary conditions. Nonreflecting characteristic boundary conditions developed by Thompson[17] are used at the inflow, outflow boundaries in the streamwise direction and the far side boundary in the radial direction. It was found necessary to use a sponge layer[13] next to the outflow boundary to control spurious wave reflections from the outside of the computational domain. The strategy of using a sponge layer at the end of the domain is similar to that of the sponge region or exit zone used by others,[3,12] which has been proved to be very effective to control the wave reflections through the outflow boundary. The computational results in the sponge layer are not truly physical and therefore are not used in the data analysis.

For the axisymmetric jet a hyperbolic tangent mean velocity profile is specified at the inlet $x=0$, which is given by

$$\bar{u}_x = \frac{U_0}{2}\left\{1-\tanh\left[\frac{R_0}{4\delta_2}\left(\frac{r}{R_0}-\frac{R_0}{r}\right)\right]\right\} + \frac{U_1}{2}\left\{1-\tanh\left[\frac{R_1}{4\delta_2}\left(\frac{|r-2R_0|}{R_1}-\frac{R_1}{|r-2R_0|}\right)\right]\right\} \tag{12}$$

where U_0 and U_1 stand for the maximum mean velocities of the primary and secondary jet streams at the inlet respectively, $R_1=(U_1/U_0)R_0$ stands for the radius of the secondary jet stream of the coaxial jets, and $\delta_2=0.1R_0$ is chosen to be the initial momentum thickness.[18] For the single cold and hot jets $U_1=0$. For the coaxial jets the secondary jet stream is located around $r=2R_0$ at the inlet. The flowfield is initiated with this longitudinal velocity profile, while the initial radial velocity is taken as zero.

The inlet temperature profile is specified by the Crocco–Busemann relation,[19] given by

$$T = M^2\frac{\gamma-1}{2}\left(U_0\bar{u}_x-\bar{u}_x^2\right)+\frac{T_0-T_a}{U_0}\bar{u}_x+T_a \tag{13}$$

where T_0 and T_a represent the jet centerline temperature and the ambient temperature, respectively. Initially, the pressure field is assumed to be uniform.

At the inflow boundary the flow is perturbed to induce the roll up and pairing of vortex rings.[20] The perturbation is given by the eigenfunctions obtained from linear stability theory. The frequencies chosen are the most unstable mode f_0 for the single jet without temperature difference and its first two leading subharmonics, $f_0/2$ and $f_0/4$. For the velocity profile given by Eq. (12) with $\delta_2=0.1R_0$, the nondimensional fundamental frequency used in the simulations is the same as that of Mitchell et al.,[3] which is $f_0R_0/U_0=0.21$.

B. Solution of Lilley's Equation

For the numerical solution of Eq. (8), it is convenient to define

$$\Pi_1=\Pi,\qquad \Pi_2=\frac{\mathrm{D}\Pi}{\mathrm{D}t},\qquad \Pi_3=\frac{\mathrm{D}^2\Pi}{\mathrm{D}t^2}-\frac{1}{r}\frac{\partial}{\partial x_i}\left(rc^2\frac{\partial\Pi}{\partial x_i}\right) \tag{14}$$

The initial values of Π_1, Π_2, and Π_3 are taken as zero, corresponding to the initial conditions for the flowfield of the DNS.

From the combination of Eq. (8) and the definitions given in Eq. (14), the governing equations about Π_1, Π_2, and Π_3 can be given as

$$\frac{\partial\Pi_1}{\partial t}=\Pi_2-u_x\frac{\partial\Pi_1}{\partial x}-u_r\frac{\partial\Pi_1}{\partial r} \tag{15}$$

$$\frac{\partial\Pi_2}{\partial t}=\Pi_3-u_x\frac{\partial\Pi_2}{\partial x}-u_r\frac{\partial\Pi_2}{\partial r}+c^2\nabla^2\Pi_1+\frac{\partial c^2}{\partial x}\frac{\partial\Pi_1}{\partial x}+\frac{\partial c^2}{\partial r}\frac{\partial\Pi_1}{\partial r} \tag{16}$$

$$\begin{aligned}\frac{\partial\Pi_3}{\partial t}=&-u_x\frac{\partial\Pi_3}{\partial x}-u_r\frac{\partial\Pi_3}{\partial r}\\&-2c^2\left[\frac{\partial u_x}{\partial x}\frac{\partial^2\Pi_1}{\partial x^2}+\left(\frac{\partial u_x}{\partial r}+\frac{\partial u_r}{\partial x}\right)\frac{\partial^2\Pi_1}{\partial x\partial r}+\frac{\partial u_r}{\partial r}\frac{\partial^2\Pi_1}{\partial r^2}\right]\\&-2c^2\frac{u_r}{r^2}\frac{\partial\Pi_1}{\partial r}-2\frac{\partial c^2}{\partial x}\left(\frac{\partial u_x}{\partial x}\frac{\partial\Pi_1}{\partial x}+\frac{\partial u_x}{\partial r}\frac{\partial\Pi_1}{\partial r}\right)\\&-2\frac{\partial c^2}{\partial r}\left(\frac{\partial u_r}{\partial x}\frac{\partial\Pi_1}{\partial x}+\frac{\partial u_r}{\partial r}\frac{\partial\Pi_1}{\partial r}\right)-2\gamma\left(\frac{\partial u_x}{\partial x}\frac{\partial u_x}{\partial x}+2\frac{\partial u_x}{\partial r}\frac{\partial u_r}{\partial x}\right.\\&\left.+\frac{\partial u_r}{\partial r}\frac{\partial u_r}{\partial r}\right)\left(\frac{\partial u_x}{\partial x}+\frac{\partial u_r}{\partial r}\right)-2\gamma\frac{u_r^3}{r^3}\end{aligned} \tag{17}$$

The spatial differentiation in Eqs. (15–17) is performed by the sixth-order compact finite difference scheme as that used for the DNS. Equations (15–17) are time marched to obtain Π_1, Π_2, and Π_3 using the Runge–Kutta scheme as that for the DNS of the flowfield. In this study artificial damping terms are used in the time marching as other commonly used CAA schemes to solve the aeroacoustic equation in time.[21] The addition of damping terms helps to stabilize the solution. A second-order explicit damping in the form of $\varepsilon\nabla^2\Pi_i$ is added explicitly to the right-hand side of Eqs. (15–17) with $i = 1, 2, 3$ respectively, where ε is the damping coefficient that has been kept to a minimum value to reduce the adverse effects of damping on the solution accuracy. In the simulations keeping the resolution high relative to the dominant sound wavelengths emitted by the axisymmetric jet meant that the artificial viscosity effect on these sound waves was insignificant. This was confirmed by varying the artificial viscosity coefficient and by the reasonable agreement achieved with the DNS.

The first-order wave equations are used as the boundary conditions for the axisymmetric Lilley's equation, which were found to be sufficient for the cases studied. These simple first-order wave equations at the domain boundaries can be written as

$$\frac{\partial \Pi_i}{\partial t} + (u - c)\frac{\partial \Pi_i}{\partial x} = 0, \qquad \text{at} \qquad x = 0 \tag{18}$$

$$\frac{\partial \Pi_i}{\partial t} + (u + c)\frac{\partial \Pi_i}{\partial x} = 0, \qquad \text{at} \qquad x = L_x \tag{19}$$

$$\frac{\partial \Pi_i}{\partial t} + c\frac{\partial \Pi_i}{\partial r} = 0, \qquad \text{at} \qquad r = L_r \tag{20}$$

where $i = 1, 2, 3$ is the subscript and u and c are the local axial velocity and sonic speed, respectively.

IV. Results and Discussion

In the simulations performed, the considered jet Mach number is $M = 0.8$, which is based on the initial centerline velocity of the primary jet stream and the ambient temperature. The flow considered is a low-Reynolds-number flow with $Re = 2.5 \times 10^3$, which is based on the primary jet radius. The Prandtl number considered is $Pr = 1.0$. The dynamic viscosity is chosen to be temperature dependent according to $\mu = \mu_a(T/T_a)^{0.76}$, and the ratio of specific heats used is $\gamma = 1.4$. The dimensions of the computational box used are $L_x = 85R_0$ with $L_{xp} = 70R_0$, and $L_r = 80R_0$, where $L_{xp} < x \le L_x$ is the sponge layer. The grid system used is of 1701×570 nodes. The grid has a uniform distribution in the streamwise direction, while it is stretched in the radial direction to include a sufficient number of points in the jet shear layer. In this study a grid-independence test has been performed, following the grid-refinement study performed in a previous study to determine the optimum number of grids.[13] In the simulations the time step was limited by the Courant–Friedrichs–Lewy (CFL) condition for stability. A CFL number of 2.0 has been used, which was tested to give time-step independent results. The results presented next are considered to be grid and time-step independent.

For simplicity, the three cases performed are referred to as case 1 ($T_0/T_a = 1$ and $U_1 = 0$), case 2 ($T_0/T_a = 1$ and $U_1/U_0 = 0.4$), and case 3 ($T_0/T_a = 2$ and $U_1 = 0$), respectively. Figure 1 shows the inlet velocity, vorticity, and temperature profiles of the three cases performed. The velocity, vorticity, and temperature profiles of cases 1 and 2 are overlapping within $r = 1$. The difference between these two cases lies in the secondary jet stream of case 2, which has different velocity and vorticity profiles. For the single hot jet (case 3) its velocity and vorticity profiles are identical to those of the single cold jet (case 1). The difference between cases 1 and 3 lies in the nonunity jet-to-ambient temperature ratio of case 3.

In each simulated case the external perturbations applied on the inflow velocities have the same frequencies, which are the most unstable mode and its first two leading subharmonics for case 1. The chosen frequencies differ from the appropriate eigenfunctions for cases 2 and 3. However, the differences are not substantial. The

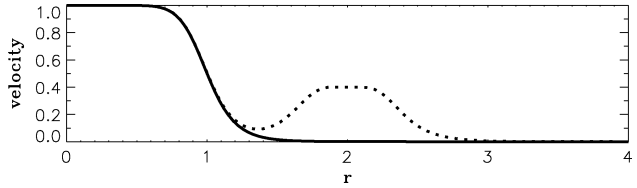

a) Inlet velocity profiles

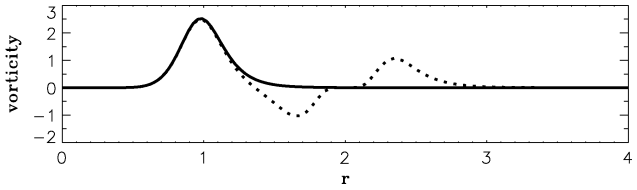

b) Inlet vorticity profiles

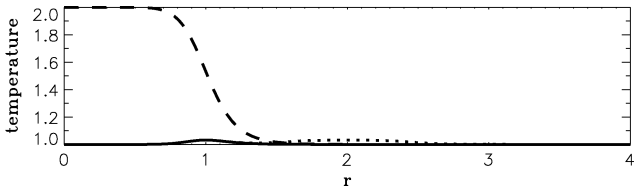

c) Inlet temperature profiles

Fig. 1 Inlet velocity, vorticity, and temperature profiles of the three cases: ——, case 1, single cold jet; · · · ·, case 2, coaxial cold jets with $U_1/U_0 = 0.4$; and – – –, case 3, single hot jet.

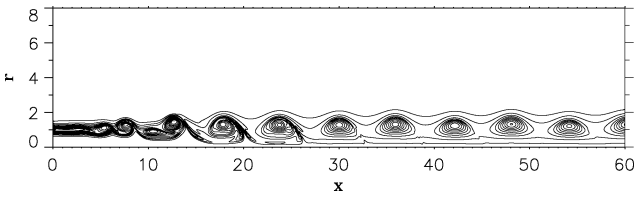

a) Case 1, single cold jet

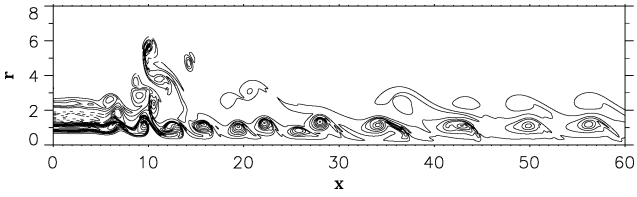

b) Case 2, coaxial cold jets

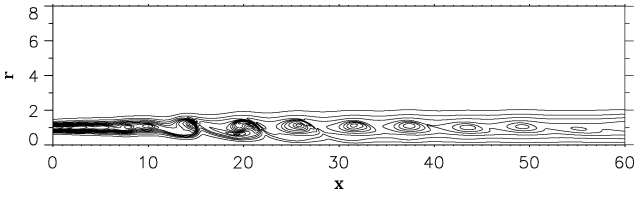

c) Case 3, single hot jet

Fig. 2 Instantaneous contours of the near field vorticity at $t = 200$ of the three cases (15 contours between the minimum and maximum).

simulations show that vortical structures are developed in each simulated case.

Because of the periodic perturbation applied at the inflow boundary, the spatially developing axisymmetric jets approach a periodic state with highly organized flow vorticity after the initial stage. Figure 2 shows the instantaneous contours of the near-field vorticity at $t = 200$ of the three cases after the periodic state has been reached. Vortex roll up can be clearly seen, and one vortex pairing is evident in Fig. 2a for the single cold jet. For the coaxial cold jets shown in Fig. 2b, it is observed that the interaction between the

secondary jet stream and the primary jet stream affects the flow vorticity significantly. The vortical flowfield of the coaxial jets spreads considerably in the radial direction at the vortex pairing/merging location. The secondary jet stream tends to enhance the flow vortical level near the jet potential core. Downstream, however, the secondary jet stream tends to elongate the vortices in the primary jet stream that weakens the flow vorticity. The presence of negative vorticity observed in Fig. 2b for the coaxial jets is associated with the vorticity profile specified at the inflow boundary, which has negative values, as shown in Fig. 1b. Comparing the single hot jet with the cold jet, it is observed that the flow becomes less vortical when the jet-to-ambient temperature ratio increases. The flow vorticity is insignificant downstream in Fig. 2c for the hot jet. This is because that high temperature tends to stabilize the jet because of the increase in viscosity.

The simulations performed are instantaneously axisymmetric; therefore, three-dimensional instabilities were inhibited. Because of the axisymmetric nature of the simulations, the large-scale vortical structures in the flowfield do not break down as they would in fully three-dimensional turbulent jets. The spreading of the purely axisymmetric jets is also smaller than that of three-dimensional jets caused by the lack of vortex breakdown. The strictly axisymmetric jet simulated here differs from a fully three-dimensional jet that is axisymmetric in its mean flow. A direct comparison between the simulated data and experimental measurements with the same flow conditions is not possible. However, the results for case 1 agree very well with those in the literature.[3]

Vortical structures in jet shear layers act as sound sources, which radiate sound to the jet far field. Figure 3 shows the instantaneous sound-field predictions of the three cases from the DNS and solution of Lilley's equation. It is observed that the acoustic field produced by the vortical structures is highly directive. The propagating sound waves are primarily beamed with a distinctive angle relative to the jet streamwise direction. At a certain radial location the sound distribution is highly nonuniform, which indicates complex sound source structures in the axisymmetric jets. Qualitatively there is no significant difference in the sound radiation pattern between cases 1 and 2. The sound field of the single hot jet (case 3), however, becomes more directed in the axial direction with a longer sound wave length compared with the cold jets. The longer sound wave length in the hot jet is mainly associated with the larger sound speed in the jet shear layer. The sound wave length can be calculated as $\lambda = c/f$, where f stands for frequency. In the hot jet larger sound speed leads to longer wave length in the shear layer for a certain frequency. This in turn leads to longer sound wave length in the jet far field because the sound is emitted from the jet shear layer. The enhanced directionality of the hot jet is perhaps caused by the shorter sound source of the hot jet as shown below. In Fig. 3 it is noticed that the sound predictions from Lilley's equation show similar patterns to those from the DNS.

An advantage offered by DNS as a tool of CAA is that it yields the complete flowfield and the exact structure of the sound source, which are hard to get from experimental measurements. In this study time-averaged quantities are calculated to examine the mean flowfields and the statistic sound source distributions. To check the usual assumption of a time-independent parallel base flow made for the jet when Lilley's acoustic analogy was applied to jet noise calculations,[8,10,12] Fig. 4 shows the time-averaged streamwise velocity contours of the three cases from the DNS. The time interval used for the averaging is between $t_1 = 140.0$ to $t_2 = 216.2$ after the flow has reached the periodic stage that includes 16 periods of the fundamental frequency. For the coaxial jets it is noticed that the merging of the secondary jet stream with the primary jet stream affects the growth of the jet shear layer and the flowfield spreads more in the radial direction than the single jets. For all of the three cases, it is obvious that the mean flow can be roughly considered to be parallel after the vortex pairing/merging locations at about $x = 15$. Before the vortex pairing/merging locations, the mean flow spreads in the radial direction as a result of the initial growth of the shear layer that invalidates the parallel mean flow assumption. This, however, does not cause any problem in the acoustic modeling performed here because the nonlinearized Lilley's equation is

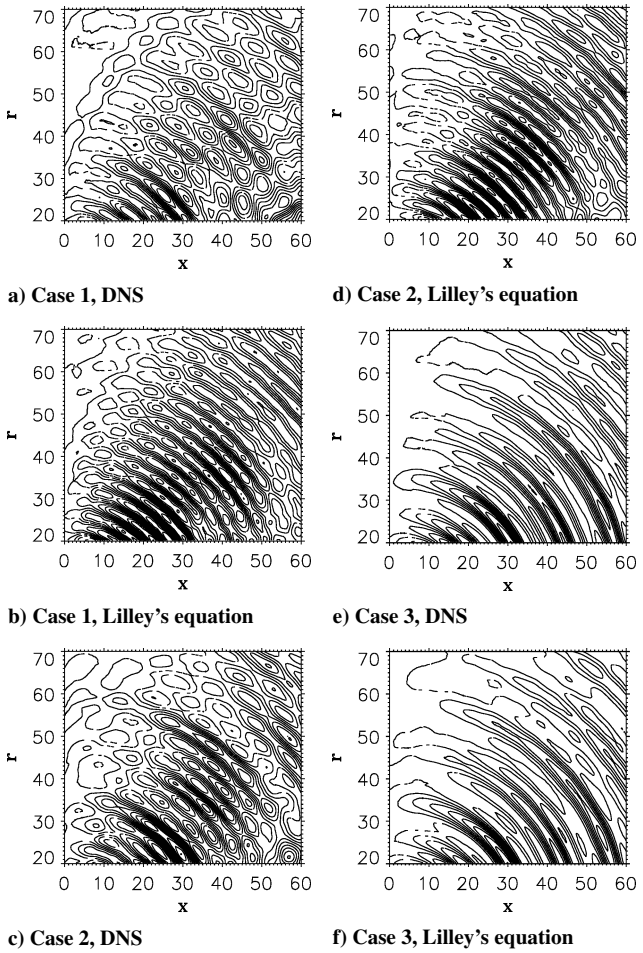

Fig. 3 Far-field sound predictions from the DNS and solution of Lilley's equation: pressure fluctuation at $t = 200$ of the three cases (15 contours between the minimum and maximum).

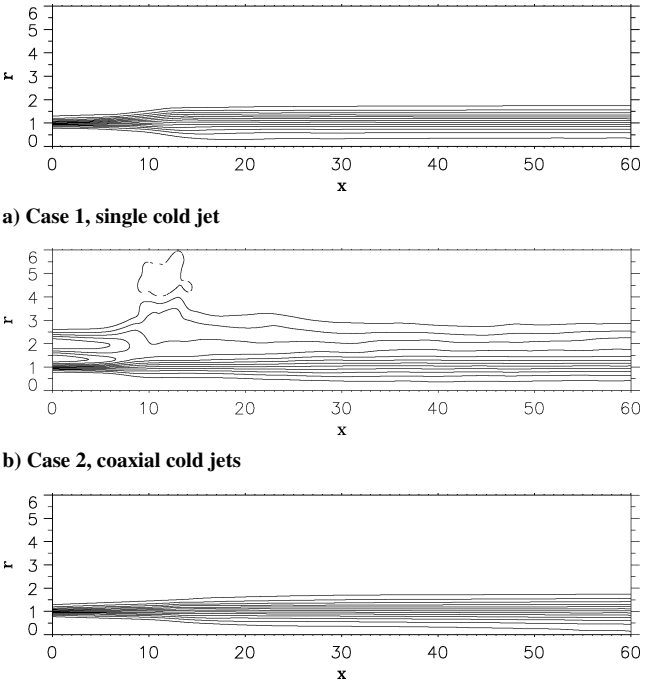

Fig. 4 Time-averaged streamwise velocity contours of the three cases (15 contours between the minimum and maximum).

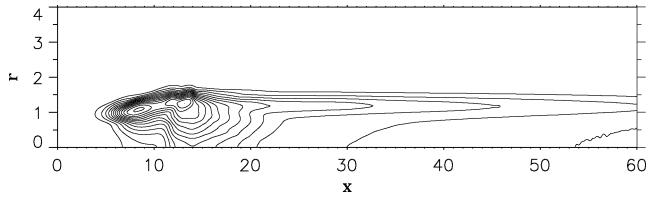

a) Case 1, single cold jet

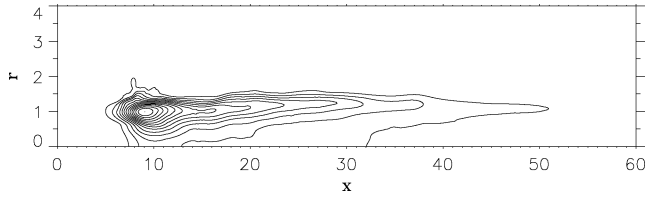

b) Case 2, coaxial cold jets

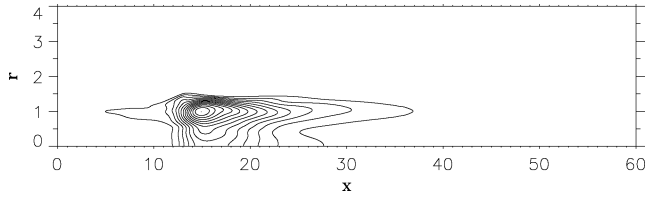

c) Case 3, single hot jet

Fig. 5 Contours of the rms of the sound source fluctuation of the three cases (15 contours between the minimum and maximum).

adopted in this study through which the jet spreading and merging effects can be taken into account.

The right-hand side of Lilley's equation is considered to be the sound source. Instantaneously, its value can be positive or negative. To examine the statistical sound source distribution, contours of the rms of the sound source fluctuation are shown in Fig. 5. The rms of the fluctuation of a quantity φ is calculated as $(\overline{\varphi'^2})^{1/2} = (\overline{\varphi^2} - \overline{\varphi}^2)^{1/2}$. Here, the quantity examined is the right-hand side of Eq. (8). It can be seen that the intense sound source is located near the end of the jet potential core where vortex pairing/merging occurs. The acoustic source has a long axial length in the streamwise flow direction. Compared with the source of the single jet, the sound source of the coaxial jets has a smaller spatial distribution. This is mainly because the secondary jet stream weakens the flow vorticity downstream as shown in Fig. 2. Between the two single jets the hot jet (case 3) has a much smaller sound source than the cold jet (case 1) because of the weaker vorticity as evident in Fig. 2.

For clarity, Fig. 6 shows a comparison of the profiles of the axial and radial distributions of the rms of the sound source fluctuation of the three cases. Although the peak values of the sound sources of the single cold jet and the coaxial cold jets do not differ from each other significantly, the sound source of the coaxial cold jets is smaller than that of the single cold jet both in the axial and radial directions. For the single hot jet its sound source is not only smaller but also considerably weaker than that of the single cold jet.

Figure 7 shows the time traces and the frequency spectra of the pressure fluctuations at a fixed point of $(x = 30, r = 30)$ in the acoustic field from the DNS and the solution of Lilley's equation for the coaxial jets with $U_1/U_0 = 0.4$. It is noticed that the pressure fluctuations obtained from the DNS and solution of Lilley's equation show a similar behavior, which fluctuates around a mean value of zero. From the frequency spectra it is evident that the sound at this point is mainly dominated by the inflow forcing frequencies. There is no obvious spectrum broadening and observable Doppler shift in frequency. This is mainly because of the axisymmetric nature of the simulations and the stationary position of the source relative to the jet potential core. In idealized axisymmetric simulations high-frequency turbulence could not develop as a result of the lack of vortex breakdown, which would have been developed in a fully three-dimensional turbulent jet. From Fig. 7 it can be seen that the

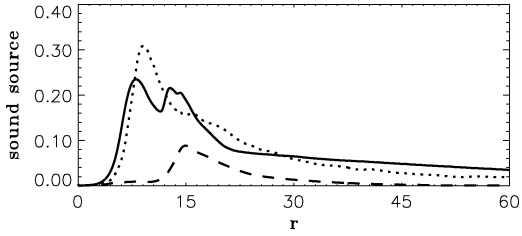

a) Axial profile at $r = 1$

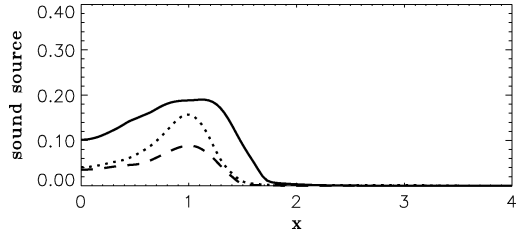

b) Radial profile at $x = 15$

Fig. 6 Profiles of the axial and radial distributions of the rms of the sound source fluctuation of the three cases: ——, case 1, single cold jet; · · · ·, case 2, coaxial cold jets with $U_1/U_0 = 0.4$; and – – –, case 3, single hot jet.

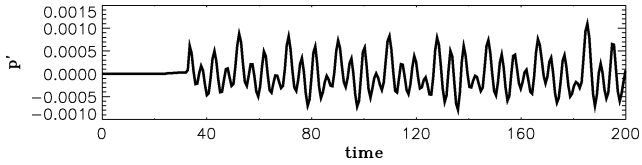

a) p' history, DNS

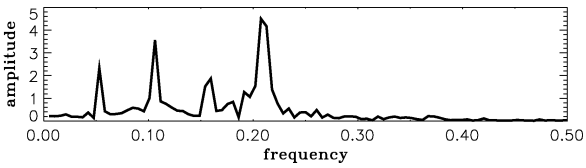

b) Fourier spetrum, DNS

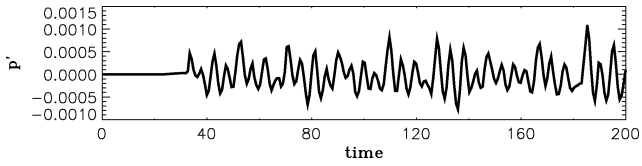

c) p' history, Lilley's equation

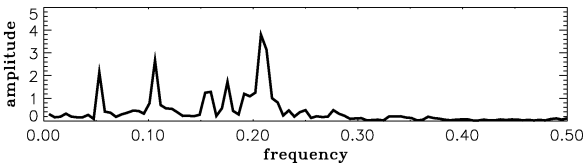

d) Fourier spectrum, Lilley's equation

Fig. 7 Time traces and the frequency spectra of the pressure fluctuations at $(x = 30, r = 30)$ from the DNS and the solution of Lilley's equation of the coaxial cold jets with $U_1/U_0 = 0.4$.

frequency spectra obtained from the DNS and the solution of Lilley's equation are in a reasonable agreement.

For the description of the energy in the radiated sound field, there are several interesting quantities.[22] One of these is the mean acoustic intensity, which is the mean rate of flow of energy per unit area caused by the acoustic disturbances. The mean acoustic intensity can be defined in terms of the mean square pressure fluctuation[22] as

$$\bar{I} \approx \frac{1}{t_2 - t_1} \int_{t_1}^{t_2} \frac{\overline{p'^2}}{\rho_a c} \tag{21}$$

where ρ_a is the ambient density. After considering the flow configuration, the total mean acoustic power output (the surface integral of the mean intensity) based on the mean acoustic intensity at a radial location r for an axisymmetric jet can be expressed as

$$\bar{P} = 2\pi r \int_{-\infty}^{\infty} \bar{I}\, \mathrm{d}x = 2\pi \int_0^{\pi} \frac{\bar{I} r^2}{\sin^2 \Theta}\, \mathrm{d}\Theta \tag{22}$$

where Θ is the spherical angle and $\Theta = 0$ points to the positive axial direction (jet downstream) while $\Theta = \pi$ points to the negative axial direction (jet upstream). In the preceding expression it is assumed that the sound source is on the symmetry axis.

The directivity of the far-field sound pressure is a useful quantity, which is a measure of the directional characteristic of a sound source. In axisymmetric jets the total mean acoustic power output can be expressed in terms of the acoustic directivity as

$$\bar{P} = 2\pi \int_0^{\pi} D(\Theta) \sin\Theta\, \mathrm{d}\Theta \tag{23}$$

where $D(\Theta)$ is the directivity of the sound field. Based on Eqs. (22) and (23), the directivity of the sound field at a radial location r for the axisymmetric jets can be given by

$$D(\Theta) = \frac{\bar{I} r^2}{\sin^3 \Theta} \tag{24}$$

Figure 8 shows a comparison of the sound field directivity distributions at $r = 60$ of the three cases from the DNS and the solution of Lilley's equation. The directivity in this figure is expressed in a logarithmic scale given by $10 \log_{10} D(\Theta)$. The apparent sound source location is taken as $x = 10R_0$ on the jet axis. It is observed that the sound radiation at lower angles (closer to the jet axis) is generally stronger than that at higher angles (away from the axis). The sound is mainly concentrated at shallow angles to the jet's downstream axis, which is consistent with Fig. 3. It is also observed that the single cold jet radiates more sound than the coaxial cold jets. This is because the sound source of the single jet has a larger spatial distribution than the coaxial jets as shown in Figs. 5 and 6. The most important feature in Fig. 8 is that the sound radiation from the single hot jet is stronger than that from the single cold jet, even though the sound source of the hot jet is smaller and weaker as shown in Figs. 5 and 6. This is mainly because of the difference in the sound speed of the two cases. As indicated in Eq. (8), the sound speed plays an important part in the sound-wave propagation. In the hot jet the large sound speed difference inside the jet shear layer affects the sound propagation considerably. The comparison between the single cold and hot jets agrees qualitatively with the comparison between a nonreacting and a reacting jet,[7] that is, high temperature tends to stabilize the jet but to enhance the sound radiation levels. Although discrepancies exist, the directivity distributions from the DNS results in Fig. 8a and the solution of Lilley's equation in Fig. 8b do not differ from each other significantly. The jagged nature of the directivity plots in Fig. 8 is mainly associated with the existence of sound beams. As shown in Fig. 3, the instantaneous sound waves are primarily beamed. The sound beams characterize the mean acoustic field that leads to a jagged directivity.

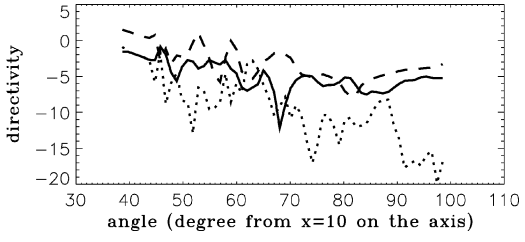

a) DNS

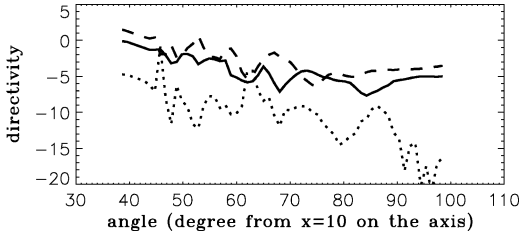

b) Lilley's equation

Fig. 8 Sound-field directivity distributions at $r = 60$ of the three cases from the DNS and the solution of Lilley's equation: ——, case 1, single cold jet; · · · ·, case 2, coaxial cold jets with $U_1/U_0 = 0.4$; and – – –, case 3, single hot jet.

The discrepancies between the solution of Lilley's equation and the DNS results shown in Figs. 3, 7, and 8 could be as a result of several reasons. First, boundary conditions for the solution of Lilley's equation and the DNS are different. Second, the viscous effects introduced in Lilley's equation (artificial viscosity) differ from the effects of the molecular viscosity in the Navier–Stokes equations for the DNS. Because the energy level of the sound field is very small, the different numerical implementations of the two methods and numerical errors can affect the agreement. Nevertheless, the agreement is acceptable as shown in the results.

V. Conclusions

In this study the sound generated by vortex pairing in subsonic axisymmetric jets is investigated by DNS and acoustic analogy based on Lilley's equation. DNS results show that the strongest sound source is located in the region where the vortex pairing/merging takes place. It is also observed that the acoustic source has a long downstream distribution. Both the DNS and numerical solution of Lilley's equation are used to predict the sound field. The results show that the acoustic field produced by the vortex pairing is highly directive, the radiated sound is mainly beamed relative to the jet centerline. The acoustic analogy solver is based on the nonlinearized third-order Lilley's equation, which is solved in the time-space domain simultaneously with the source-field calculation. The sound predictions obtained from the acoustic modeling based on the axisymmetric Lilley's equation are in reasonable agreement with the directly computed data.

Three computational cases have been performed, including a single cold jet, coaxial cold jets with the secondary/primary mean-velocity ratio $U_1/U_0 = 0.4$, and a single hot jet with the jet-to-ambient temperature ratio $T_0/T_a = 2$, respectively. It is shown that the secondary jet stream in the coaxial configuration tends to weaken the flow vorticity downstream and therefore reduce the size of the sound source. The sound radiation from the coaxial jets is consequently lower than that from the single jet. It is also observed that the sound source of the single hot jet is smaller and weaker than that of the single cold jet, but the sound radiation from the hot jet is stronger than that from the cold jet caused by the difference in sound speed. These observed trends are consistent with those from the previous studies.

The insights gleaned at this axisymmetric flow configuration can aid the understanding and predictions of sound generation from jets at more complex practical conditions such as fully three-dimensional turbulent coaxial jets. Although axisymmetric jets differ from three-dimensional turbulent jets, the methodology developed for the sound predictions from this simpler flow configuration can be very useful for the sound predictions of more complex flows.

Appendix: Lilley's Equation at the Jet Centerline

By applying l'Hôpital's rule, Lilley's equation at the jet centerline in the axisymmetric cylindrical coordinates can be written as

$$\frac{\mathrm{D}}{\mathrm{D}t}\left[\frac{\mathrm{D}^2\Pi}{\mathrm{D}t^2} - \frac{1}{r}\frac{\partial}{\partial x_i}\left(rc^2\frac{\partial \Pi}{\partial x_i}\right)\right] + 2\frac{\partial u_i}{\partial x_j}\frac{\partial}{\partial x_i}\left(c^2\frac{\partial \Pi}{\partial x_j}\right)$$

$$+ 2c^2\frac{\partial u_r}{\partial r}\frac{\partial^2 \Pi}{\partial r^2} = -2\gamma\frac{\partial u_i}{\partial x_j}\frac{\partial u_k}{\partial x_i}\frac{\partial u_j}{\partial x_k} - 2\gamma\left(\frac{\partial u_r}{\partial r}\right)^3 \tag{A1}$$

where the different terms in Eq. (A1) can be expressed as

$$\frac{1}{r}\frac{\partial}{\partial x_i}\left(rc^2\frac{\partial \Pi}{\partial x_i}\right) = c^2\left(\frac{\partial^2 \Pi}{\partial x^2} + 2\frac{\partial^2 \Pi}{\partial r^2}\right) + \frac{\partial c^2}{\partial x}\frac{\partial \Pi}{\partial x} \quad \text{(A2)}$$

$$\frac{\partial u_i}{\partial x_j}\frac{\partial}{\partial x_i}\left(c^2\frac{\partial \Pi}{\partial x_j}\right) = c^2\left(\frac{\partial u_x}{\partial x}\frac{\partial^2 \Pi}{\partial x^2} + \frac{\partial u_r}{\partial r}\frac{\partial^2 \Pi}{\partial r^2}\right) + \frac{\partial c^2}{\partial x}\frac{\partial u_x}{\partial x}\frac{\partial \Pi}{\partial x} \quad \text{(A3)}$$

$$\frac{\partial u_i}{\partial x_j}\frac{\partial u_k}{\partial x_i}\frac{\partial u_j}{\partial x_k} = \left(\frac{\partial u_x}{\partial x}\frac{\partial u_x}{\partial x} + \frac{\partial u_r}{\partial r}\frac{\partial u_r}{\partial r}\right)\left(\frac{\partial u_x}{\partial x} + \frac{\partial u_r}{\partial r}\right) \quad \text{(A4)}$$

Acknowledgment

This work was funded by the United Kingdom Engineering and Physical Sciences Research Council under Grant GR/N36097/01.

References

[1]Lilley, G. M., "On the Noise from Jets," *Noise Mechanisms*, CP-131, AGARD, 1974, pp. 13.1–13.12.

[2]Laufer, J., and Yen, T.-C., "Noise Generation by a Low-Mach-Number Jet," *Journal of Fluid Mechanics*, Vol. 134, 1983, pp. 1–31.

[3]Mitchell, B. E., Lele, S. K., and Moin, P., "Direct Computation of the Sound Generated by Vortex Pairing in an Axisymmetric Jet," *Journal of Fluid Mechanics*, Vol. 383, 1999, pp. 113–142.

[4]Dahl, M. D., and Papamoschou, D., "Analytical Predictions and Measurements of the Noise Radiated from Supersonic Coaxial Jets," *AIAA Journal*, Vol. 38, No. 4, 2000, pp. 584–591.

[5]Debiasi, M., and Papamoschou, D., "Noise from Imperfectly Expanded Supersonic Coaxial Jets," *AIAA Journal*, Vol. 39, No. 3, 2001, pp. 388–395.

[6]Fortune, V., and Gervais, Y., "Numerical Investigation of the Noise Radiated from Hot Subsonic Turbulent Jets," *AIAA Journal*, Vol. 37, No. 9, 1999, pp. 1055–1061.

[7]Zhao, W., and Frankel, S. H., "Numerical Simulations of Sound Radiated from an Axisymmetric Premixed Reacting Jet," *Physics of Fluids*, Vol. 13, No. 9, 2001, pp. 2671–2681.

[8]Morris, P. J., and Farassat, F., "Acoustic Analogy and Alternative Theories for Jet Noise Prediction," *AIAA Journal*, Vol. 40, No. 4, 2002, pp. 671–680.

[9]Lighthill, M. J., "On Sound Generated Aerodynamically: I. General Theory," *Proceedings of the Royal Society*, Vol. A211, No. 1107, 1952, pp. 564–587.

[10]Goldstein, M. E., "Aeroacoustics of Turbulent Shear Flows," *Annual Review of Fluid Mechanics*, Vol. 16, 1984, pp. 263–285.

[11]Freund, J. B., "Noise Sources in a Low-Reynolds-Number Turbulent Jet at Mach 0.9," *Journal of Fluid Mechanics*, Vol. 438, 2001, pp. 277–305.

[12]Colonius, T., Lele, S. K., and Moin, P., "Sound Generation in a Mixing Layer," *Journal of Fluid Mechanics*, Vol. 330, 1997, pp. 375–409.

[13]Jiang, X., and Luo, K. H., "Direct Numerical Simulation of the Puffing Phenomenon of an Axisymmetric Thermal Plume," *Theoretical and Computational Fluid Dynamics*, Vol. 14, No. 1, 2000, pp. 55–74.

[14]Avital, E. J., "Optimized Differentiation Schemes on Non-Uniform Grids for Computational Aeroacoustics," *Journal of Computational Acoustics*, Vol. 10, No. 3, 2002, pp. 1–15.

[15]Lele, S. K., "Compact Finite-Difference Schemes with Spectral-Like Resolution," *Journal of Computational Physics*, Vol. 103, No. 1, 1992, pp. 16–42.

[16]Williamson, J. H., "Low-Storage Runge–Kutta Schemes," *Journal of Computational Physics*, Vol. 35, No. 1, 1980, pp. 48–56.

[17]Thompson, K. W., "Time Dependent Boundary Conditions for Hyperbolic Systems," *Journal of Computational Physics*, Vol. 68, No. 1, 1987, pp. 1–24.

[18]Michalke, A., "Survey on Jet Instability Theory," *Progress in Aerospace Sciences*, Vol. 21, 1984, pp. 159–199.

[19]White, F. M., *Viscous Fluid Flow*, McGraw–Hill, New York, 1974, pp. 578–581.

[20]Sandham, N. D., "The Effect of Compressibility on Vortex Pairing," *Physics of Fluids*, Vol. 6, No. 2, 1994, pp. 1063–1072.

[21]Tam, C. K. W., "Computational Aeroacoustics: Issues and Methods," *AIAA Journal*, Vol. 33, No. 10, 1995, pp. 1788–1796.

[22]Doak, P. E., "An Introduction to Sound Radiation and Its Sources," *Noise and Acoustic Fatigue in Aeronautics*, edited by E. J. Richards and D. J. Mead, Wiley, New York, 1968, pp. 1–42.

P. Givi
Associate Editor